Chapter 2

Visualization and Characterization of Cerebrospinal Fluid Motion Based on Magnetic Resonance Imaging

Satoshi Yatsushiro, Saeko Sunohara, Hideki Atsumi, Mitsunori Matsumae and Kagayaki Kuroda

Additional information is available at the end of the chapter

http://dx.doi.org/10.5772/intechopen.73302

Abstract

Purpose: To characterize cardiac- and respiratory-driven cerebrospinal fluid (CSF) motions in intracranial space noninvasively, four-dimensional velocity mapping (4D-VM), correlation mapping, and power and frequency mapping with cardiac-gated and/or asynchronous magnetic resonance (MR) phase contrast (PC) techniques were conducted.

Methods: Cardiac-gated PC in three spatial directions was applied to young, healthy, elderly, healthy, and idiopathic normal pressure hydrocephalus patient groups. 4D-VM was created from time-resolved 3D velocity distribution represented as vector and color coding. The curl and pressure gradient were calculated. Correlation mapping provides propagation delay and correlation of CSF motion at arbitrary points regarding a reference point. In addition, asynchronous PC technique was conducted for healthy volunteers with respiratory instruction as constant rhythm. Cardiac- and respiratory-driven velocities were separated by frequency analysis. Power and frequency mapping present both the energy and dominant frequency of cardiac or respiratory CSF motion.

Results: 4D-VM, curl, pressure gradient images, and correlation mapping by cardiac-gated PC demonstrated cardiac-driven CSF motion and its propagation properties. Power and frequency mapping, correlation mapping, and displacement analysis exhibited that the cardiac-driven CSF velocity was higher than the respiratory, although the cardiac-driven displacement was smaller.

Conclusion: Visualization and characterization techniques based on PC imaging can capture the properties of CSF motion in intracranial space.

Keywords: MRI, phase contrast, cerebrospinal fluid, motion, visualization

1. Introduction

Investigations of CSF motion based on MRI have been actively performed [1–6]. CSF motion is thought to be composed of three components: cardiac-driven motion, respiratory-driven motion, and bulk flow [7, 8]. Cardiac-driven motion is primarily induced by arterial blood vessel pulsation and relates to the regulation of intracranial pressure (ICP) [2, 4, 9, 10]. A change in intrathoracic pressure caused by respiration induces the modulation of venous blood pressure, resulting in respiratory-driven motion [6, 11–14]. Bulk flow is a slow motion relating to CSF production and absorption, thus playing a role to washout wastes from the brain through the glymphatic system [7, 8, 15, 16].

Hydrocephalus is the most commonly known disease relating to the alternation of CSF dynamics through, for example, a velocity increase in the aqueduct [17–19]. Although hydrocephalus increases intracranial pressure (ICP) in some cases, normal pressure hydrocephalus (NPH), including idiopathic NPH (iNPH), does not increase ICP, and thus, it is difficult to know the exact status of the disease using invasive pressure measurement, as in a lumber puncture (LP) procedure. Even in such a case there might be abnormality in the CSF dynamics. Therefore, the investigation of the relationship between hydrocephalus and CSF motion is essential. It is also known that the development of Alzheimer's disease (AD) relates to the accumulation of amyloid beta protein and thus to the malfunction of the glymphatic system, which in turn the bulk flow [8]. Thus, the characterization of the CSF dynamics may lead to the key for clarifying the status and the symptom of the abovementioned diseases.

This chapter presents the techniques for the visualization and characterization of CSF motion in intracranial space based on the cardiac-gated PC [20, 21] and asynchronous PC technique of MRI.

2. Material and methods

The use of human subjects in this study was approved by both internal review boards of Tokai University, Kanagawa, Japan, and Tokai University Hospital, Kanagawa, Japan. All volunteers were examined after appropriate informed consent was obtained.

2.1. Cardiac-gated and asynchronous PC techniques

The cardiac-gated PC technique is the combination of continuous PC acquisition and retrospective reconstruction. A schematic diagram of the cardiac-gated PC acquisition is explained in **Figure 1(a)**. The signal is read out regardless of the electrocardiography (ECG) signal. The signals are sorted retrospectively according to the delay time from the R-wave of ECG signal to form a time series of k-space images. The k-space series are then reconstructed to be multiple PC images resulting in time-resolved velocity images. In this technique, the respiratory-induced motion is simply ignored.

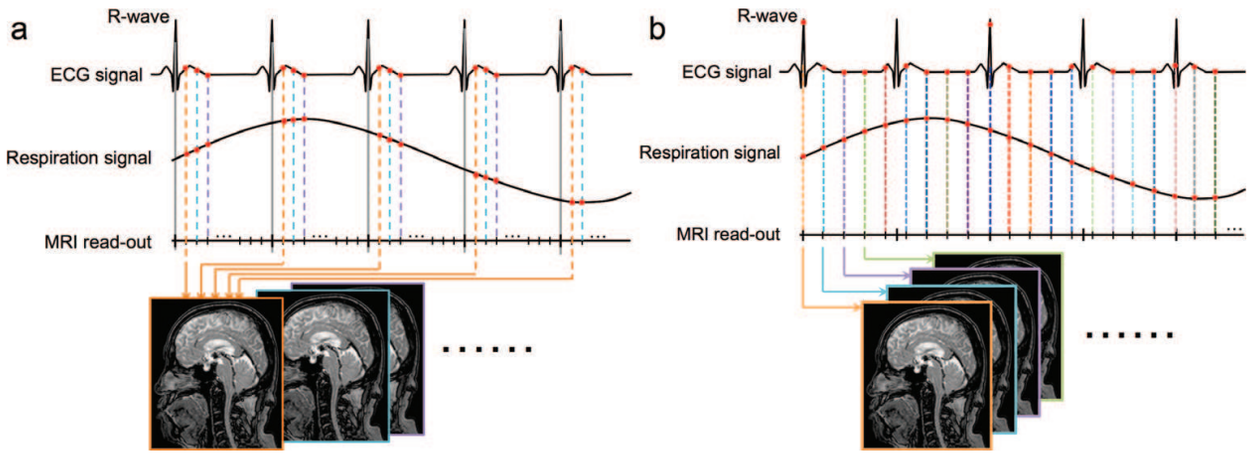

Figure 1. Schematic diagram of cardiac-gated (a) and asynchronous (b) PC acquisitions.

The asynchronous PC technique uses a rapid signal acquisition scheme, such as steady state free precession (SSFP), to obtain velocity images with the order of 217 ms per frame. When combined with the ECG and respiratory signals monitored during acquisition, this technique may simultaneously measure the cardiac- and respiratory-driven CSF velocities.

2.2. CSF motion visualization based on cardiac-gated PC imaging

Cardiac-gated PC velocity measurement was performed in three spatial directions at 1.5 T for 13 young, healthy volunteers (8 males and 5 females with mean ± SD age of 29 ± 5); 13 elderly, healthy volunteers (4 males and 9 females with mean ± SD age of 72 ± 8); and 13 patients with iNPH (2 males and 11 females with mean ± SD age of 75 ± 5). Detailed imaging conditions are shown elsewhere [10].

In segmenting the CSF space from the T2-weighted images with relatively large voxel size (approximately 1 mm^3) [22], the spatial-based fuzzy clustering method (SFCM) was applied to reduce the possible partial volume effect [23]. This method differentiated tissues with different signal intensities even in an identical voxel and determined the boundary between the tissues, resulting in a reasonably segmented image.

2.3. Four-dimensional velocity mapping

Four-dimensional velocity mapping (4D-VM) visualizes the cardiac-driven CSF motion in intracranial space, which is composed of cardiac-gated PC acquisition in three spatial directions. In-plane velocities were indicated as arrows, while out-plane velocities were color-coded. The time-resolved velocity maps or 4D-VM were superimposed on T2 images.

2.3.1. Curl of the velocity field

In general, a vector field is fully characterized by the divergence and curl of the velocity field based on Helmholtz's theorem [24]. The curl of the velocity field was calculated as follows to provide the intensity of the vortex:

$$curl\ \mathbf{v} = \nabla \times \mathbf{v} \tag{1}$$

where **v** is the velocity vector fields in the spatial directions and ∇ is a spatial differential operator called nabla.

2.3.2. Pressure gradient

The pressure gradient was calculated based on the Navier-Stokes equation as follows:

$$\nabla P = -\rho\left(\frac{\partial \mathbf{v}}{\partial t} + (\mathbf{v}\cdot\nabla)\mathbf{v}\right) + \mu\nabla^2\mathbf{v} \tag{2}$$

where ∇P is the pressure gradient [Pa/m]; ρ is the fluid density [kg/m^3], which is 1.007×10^3 in the case of the CSF; and μ is the dynamic viscosity [Pa s], 1.1×10^{-3} for CSF. The first term in the right-hand side of the equation is composed of acceleration. The second is of convection, and the third is of viscosity. Although the pressure gradient is a vector, the absolute of the pressure gradient vector was mapped as color-scale for simplicity.

2.4. Correlation mapping

Correlation mapping is a technique to provide the delay and correlation of CSF motion propagation in space. This technique works under the assumptions that CSF moves with pressure propagating from the pulsation of blood vessels and/or brain parenchyma and that CSF itself is a media of such pressure propagation.

The velocity waveform of CSF motion or blood flow obtained by the time-resolved PC acquisition was sampled at a particular reference point. By time shifting the velocity waveform at an arbitrary point to have the highest correlation coefficient with that at the reference, as illustrated in **Figure 2**, two important parameters, $d_{\max}$ and $P_{d_{\max}}$ may be calculated. The following equation was used to calculate these values assuming that the lengths and shapes of the waveforms are similar to each other and that there is a linear delay between the waveforms:

$$P_d = \frac{\sum_{k=1}^{N}\left(v_{R_k} - \overline{v}_R\right)\left(v_{A_{k-d}} - \overline{v}_A\right)}{\sum_{k=1}^{N}\sqrt{\left(v_{R_k} - \overline{v}_R\right)^2\left(v_{A_{k-d}} - \overline{v}_A\right)^2}} \quad d = \left(0, 1, 2, \cdots, N-1\right) \tag{3}$$

where P_d is the correlation coefficient with the number of delay time points d within a cardiac period, v_{R_k} is the velocity of the reference waveform, $\overline{v}_R$ is the average of v_{R_k}, $v_{A_{k-d}}$ is the velocity at the arbitrary spatial location and shifted for d points with respect to the original, $\overline{v}_A$ is the average of $v_{A_{k-d}}$, k is the time index, and N is the total number of data points and thus the number of images, within a cardiac period. Eq. (3) is similar to but different from that used in the pulsatility-based segmentation (PUBS) [25]. The delay giving the maximum correlation

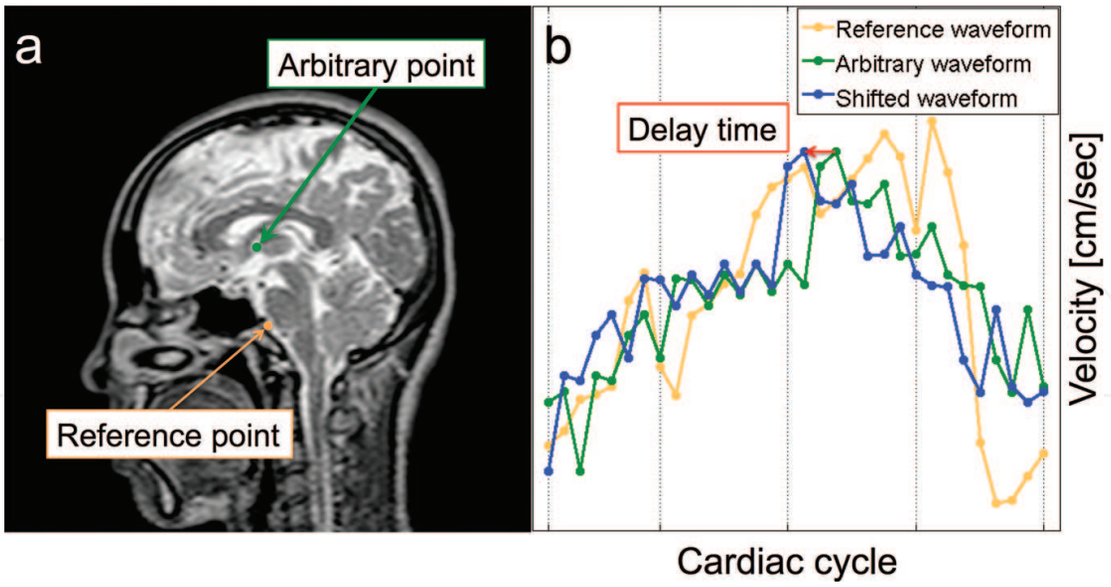

Figure 2. A reference point and an arbitrary point for observing a correlation of CSF velocity waveforms are shown on a T_2-weighted image (a). A waveform at an arbitrary point (green line) was shifted (blue line) to maximize the correlation coefficient with that of the reference (orange line) as shown in (b). The amount of the shift indicated by an arrow was defined as the "delay time," whereas the maximum correlation value was defined as the "maximum correlation."

$P_{d_{\max}}$ was defined as the delay time $d_{\max}$, Then $d_{\max}$ and $P_{d_{\max}}$ were estimated and mapped for all voxels in the CSF space.

After validating the appropriateness of the correlation mapping technique in a flow phantom [10], it was applied to three subject groups. The reference region was set at CSF near the basilar artery in the midline slice to visualize CSF motion propagation derived from the cardiac pulsation [9]. The CSF motion propagation in the FH direction was analyzed because the dominant motion was expected to be to and fro in this direction.

2.5. Cardiac- and respiratory-driven CSF motion characterized by asynchronous PC imaging

Asynchronous 2D-PC imaging in the sagittal plane in the midline was applied to 12 healthy volunteers (10 males and two females with mean ± SD age of 31 ± 13 years old) using 3 T-MRI. Each volunteer was instructed to have 6-s cycle by homemade audio guidance. In addition, 10- and 16-s cycle respiration was also instructed for seven healthy volunteers (six males and one female with mean ± SD age of 31 ± 12 years old). Cardiac and respiratory signals were measured by ECG and a bellows-type pressure sensor on the volunteer's abdomen. Detailed imaging conditions can be found elsewhere [13]. Non-gated, PC image acquisition with 217-ms (4.61 frame/s) temporal resolution was repeated 256 times, resulting in about 56-s total acquisition time for each volunteer.

2.6. Power and frequency mapping

Since cardiac- and respiratory-driven CSF motions have different frequency ranges corresponding to cardiac pulsation and respiration, these motions should appear as different spectral peaks in the frequency domain. Monitoring an ECG signal as well as a respiratory signal, which

is obtained by a bellows-type pressure sensor, the cardiac- and respiratory-driven CSF velocity components were separately extracted in the frequency domain. The energy of the cardiac and respiratory component was calculated by integrating the power spectral density of these components in each voxel and then normalized by the entire energy in the 0–2.0-Hz range. Such calculations were performed for all the voxels including CSF to create a power map (P-map). The frequencies of the maximum peak in the PSD were depicted at all the voxels to form a frequency map (F-map). The brightness of the F-map was weighted with that averages the maximum values of PSD in intracranial space. To quantify the P-map, regions of interest (ROIs) were placed, as shown in **Figure 3**.

2.7. Pressure gradient

The pressure gradient of the cardiac- and respiratory-driven CSF velocity along the FH direction was calculated based on Eq. (2). The average of the positive (caudal-to-cranial) and negative (cranial-to-caudal) peak pressure gradient was quantitatively analyzed in ROIs.

2.8. Correlation mapping

The correlation mapping technique described in the previous section was applied to the cardiac and respiratory velocities of individual volunteers with the reference region set at the spinal subarachnoid space. The maximum correlation and delay time of each motion component were obtained at the ROIs located at the prepontine, aqueduct, fourth ventricle, and lateral ventricle.

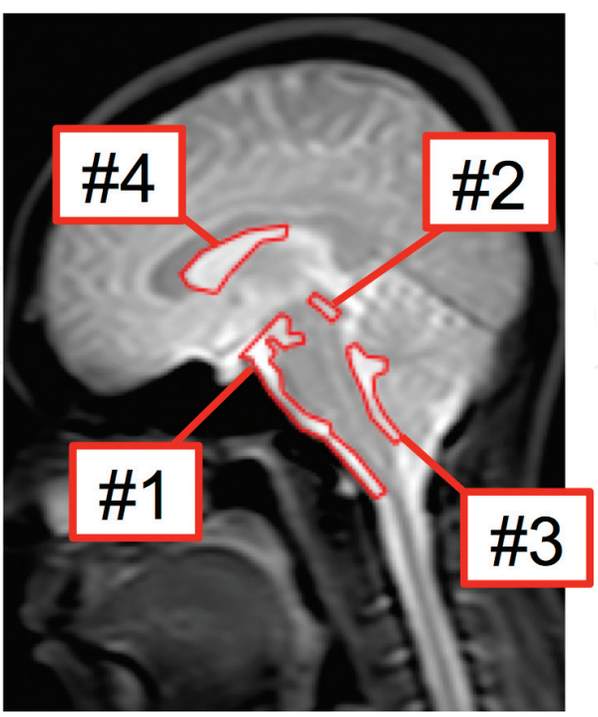

Figure 3. A T2 image of a healthy subject with ROIs: (#1) the anterior cistern of the brainstem, (#2) aqueduct, (#3) fourth ventricle, and (#4) lateral ventricle.

2.9. Displacements of cardiac- and respiratory-driven CSF motion

The displacements of the cardiac and respiratory velocity waveforms were calculated. The displacement was regarded to be during the diastolic or inhalation period when a slope of the velocity waveform was positive and to be during the systolic or exhalation period when a slope was negative. Thus, the displacements were calculated with following equations in the ROIs specified above:

$$D_{dia/inh} = \frac{1}{N}\sum_{n=1}^{N}\left(\sum_{m=1}^{M_{dia/inh}} \left|v\left(m\cdot\Delta t\right)\right|\Delta t\right)_n \tag{4}$$

$$D_{sys/exh} = \frac{1}{N}\sum_{n=1}^{N}\left(\sum_{m=1}^{M_{sys/exh}} \left|v\left(m\cdot\Delta t\right)\right|\Delta t\right)_n \tag{5}$$

where $D_{dia/inh}$ is the CSF displacement during diastole or inhalation, $D_{sys/exh}$ are the displacement during systole or exhalation, $M_{dia/inh}$ and $M_{sys/exh}$ are the number of data points during each physiological state, N is the number of cardiac or respiratory cycles in the observation duration, v is cardiac- or respiratory-driven CSF velocity, and Δt is the temporal resolution.

3. Results

3.1. CSF motion visualization based on cardiac-gated PC imaging

The Reynolds number in the aqueduct was calculated to be around 136 when the velocity was 2.47 cm/s. Since this value was less than 2000, the CSF motion inside the aqueduct was regarded to be a laminar flow when moving toward one direction. The 4D-VM images of the cardiac-driven CSF motion of a healthy volunteer and iNPH patient are shown in **Figure 4**, demonstrating the difference in the velocity distribution between the healthy volunteer and the iNPH patient. The peak-to-peak velocity in the healthy volunteers in the aqueduct was 1.25 ± 0.78 [cm/s], while that in the iNPH patients was 2.86 ± 1.39 [cm/s]. The curl images in **Figure 5** showed that the disturbance around the brainstem in the iNPH patient was higher than that of the healthy volunteer. The intensity of the aqueduct curl was 3.32 ± 1.63 [$(s\ cm^2)^{-1}$] in the healthy volunteers and 14.00 ± 6.87 [$(s\ cm^2)^{-1}$] for the patients. The pressure gradient images in **Figure 6** revealed that the pressure gradient in the iNPH patient around the brain stem was larger than the healthy. In the same region, the pressure gradient was 147.04 ± 97.48 [Pa/m] for the healthy volunteers and 615.66 ± 397.46 [Pa/m] for the patients.

The delay time and maximum correlation maps in **Figure 7** exhibited that the delay and maximum correlation maps for a young, healthy subject differed according to the CSF motion propagation. The result for an elderly, healthy subject looked like similar but slightly different in longitudinal cerebral fissure from the young, healthy subject.

The velocity waveforms obtained from the prepontine, foramen magnum, third ventricle, fourth ventricle, lateral ventricle, and longitudinal fissure, and those power spectra are shown

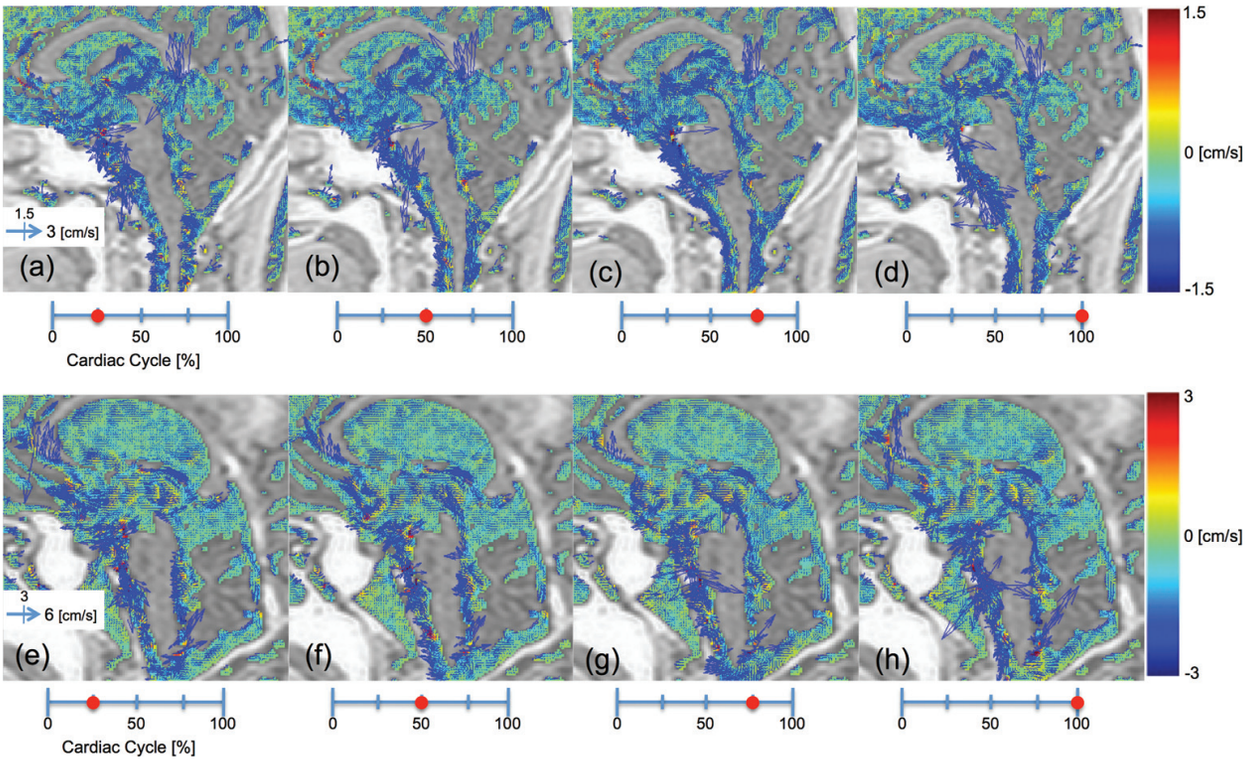

Figure 4. Four-dimensional velocity images of the cardiac-driven CSF motion of a healthy volunteer (a–d) and an iNPH patient (e–h) in a cardiac cycle.

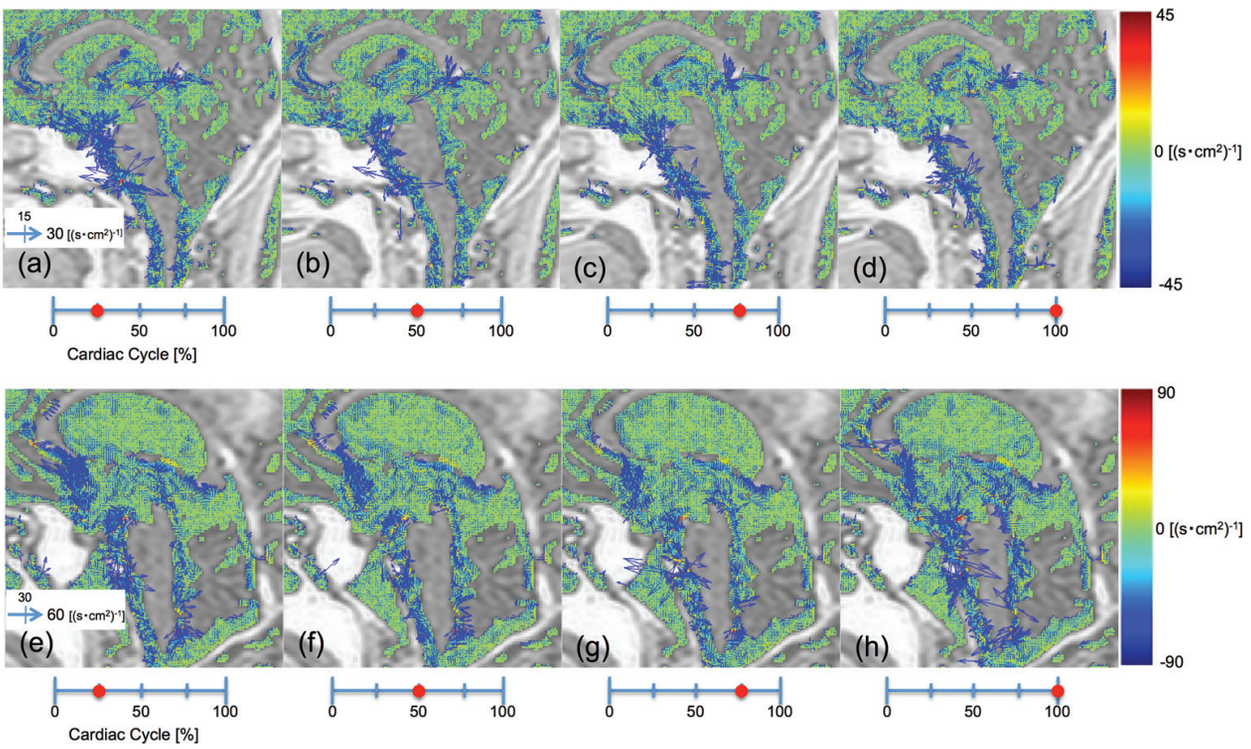

Figure 5. Curl distributions of the cardiac-driven CSF motion of a healthy volunteer (a–d) and an iNPH patient (e–h) in a cardiac cycle.

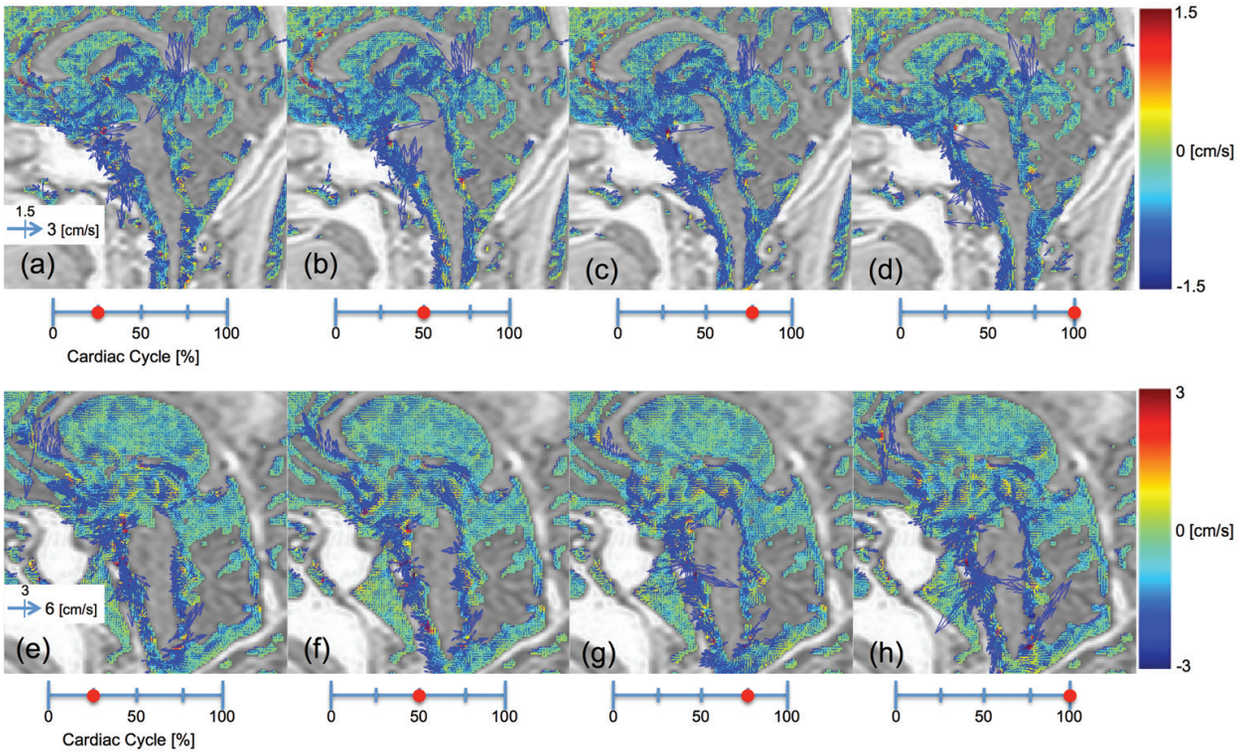

Figure 6. Pressure gradient of the cardiac-driven CSF motion of a healthy volunteer (a–d) and an iNPH patient (e–h) in a cardiac cycle.

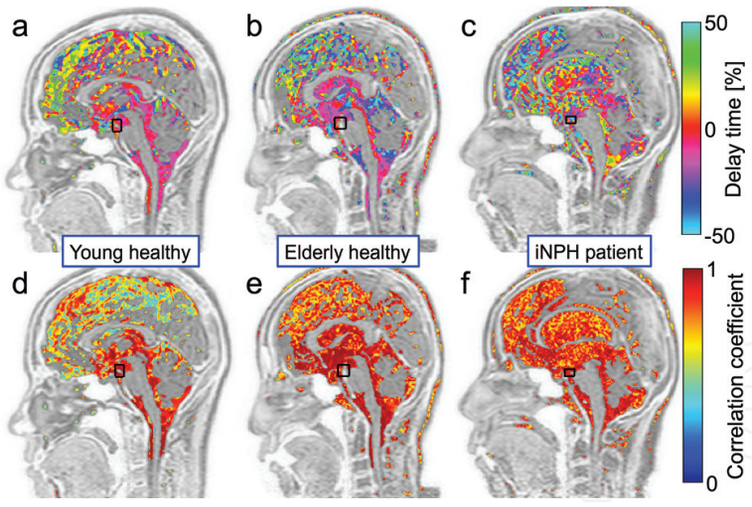

Figure 7. (a–c) are delay time maps, and (d–f) are maximum correlation maps. The black rectangles indicate the reference region. The delay and maximum correlation maps demonstrated propagation properties of CSF motion with different status.

in **Figure 8**. The dominant frequency of the motion in the regions was identical to the cardiac pulsation frequency (≈1.08 Hz). The delay times at the ROIs without the foramen magnum and longitudinal cerebral fissure were quantified, while the mean deviation of the delay was calculated and is summarized in **Table 1**. The mean deviation exhibited a difference of CSF motion propagation among the three subject groups.

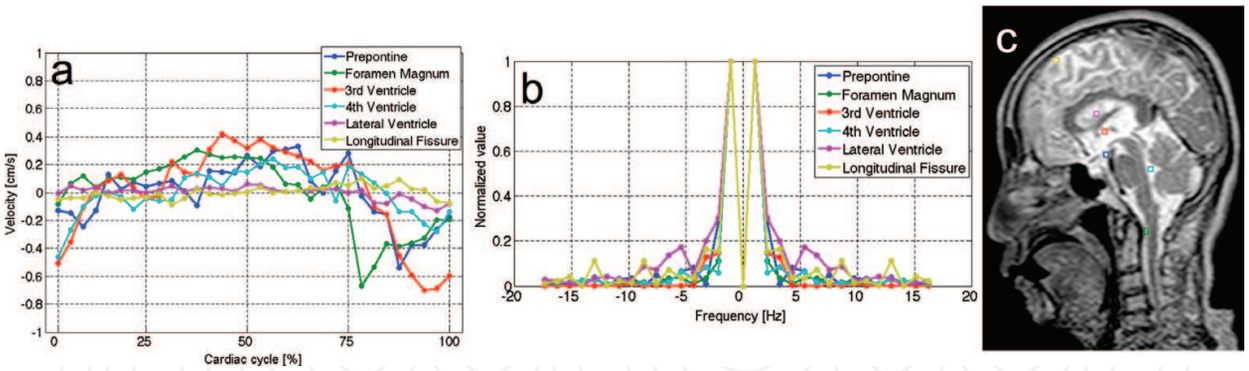

Figure 8. Results for the primary frequency components of the CSF motion propagation. (a) Velocity waveforms are shown at various tissue regions indicated by color squares on T2 image (c). (b) Power spectra of those waveforms normalized by each peak are exhibited.

	Prepontine	Third V[a]	LV[b]	Fourth V[c]	MD[d]
Young, healthy	0.90 ± 2.61	7.03 ± 6.47	12.01 ± 7.69	10.18 ± 9.41	14.25
Elderly, healthy	−0.37 ± 2.82	5.02 ± 6.05	4.56 ± 6.99	5.22 ± 11.86	7.96
iNPH	−0.59 ± 3.88	2.24 ± 3.41	0.92 ± 5.36	2.75 ± 4.41	4.65

[a]Third V, third ventricle
[b]LV, lateral ventricle
[c]Fourth V, fourth ventricle
[d]MD, mean deviation. The rightmost column is the MD of the delay time fraction among the different regions, indicating the variety of the delay time in the intracranial space in each subject group.

Table 1. Fraction of the delay time [%] of CSF motion propagation in a cardiac cycle at the prepontine, third ventricle, lateral ventricle, and fourth ventricle.

The quantification of the average and standard deviation of the maximum correlation coefficient distribution in the intracranial CSF space segmented by the SFCM with manual segmentation is shown in **Figure 9**. Significant differences between the young, healthy group and the others are shown; in addition, the standard deviation of the maximum correlation distribution in the same region indicates significant differences among all groups.

3.2. Cardiac- and respiratory-driven CSF motion characterized by asynchronous PC imaging

Figure 10(a) presents the CSF velocity waveform at a voxel obtained by asynchronous 2D-PC imaging; **Figure 10(b)** is power spectra of the CSF (blue line), ECG (red), and respiratory signal (green); and **Figure 10(c)** is the separated cardiac and respiratory CSF velocities. **Figure 11** represents the cardiac and respiratory P-maps as well as F-map of a healthy volunteer under a 6-s respiratory cycle. The cardiac components were high at the spinal subarachnoid space and anterior cistern of brainstem, while the respiratory components were relatively small in same regions. The F-map showed that the cardiac component around 1 Hz was dominant at the anterior cistern of the brainstem, while various frequencies were intermixed at the frontal horn

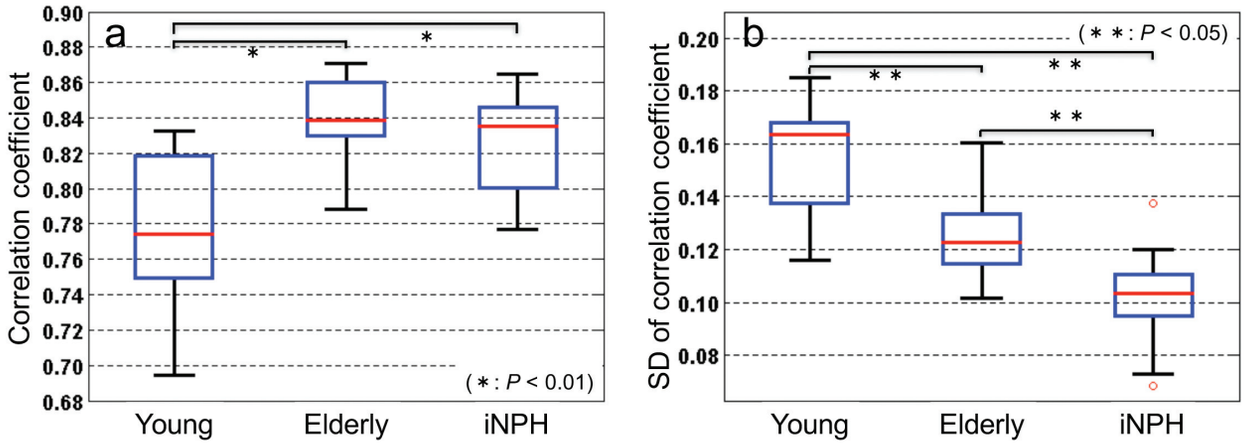

Figure 9. Boxplot of the mean correlation coefficient in the intracranial CSF space for the three subject groups is shown in (a) and the standard deviation (b).

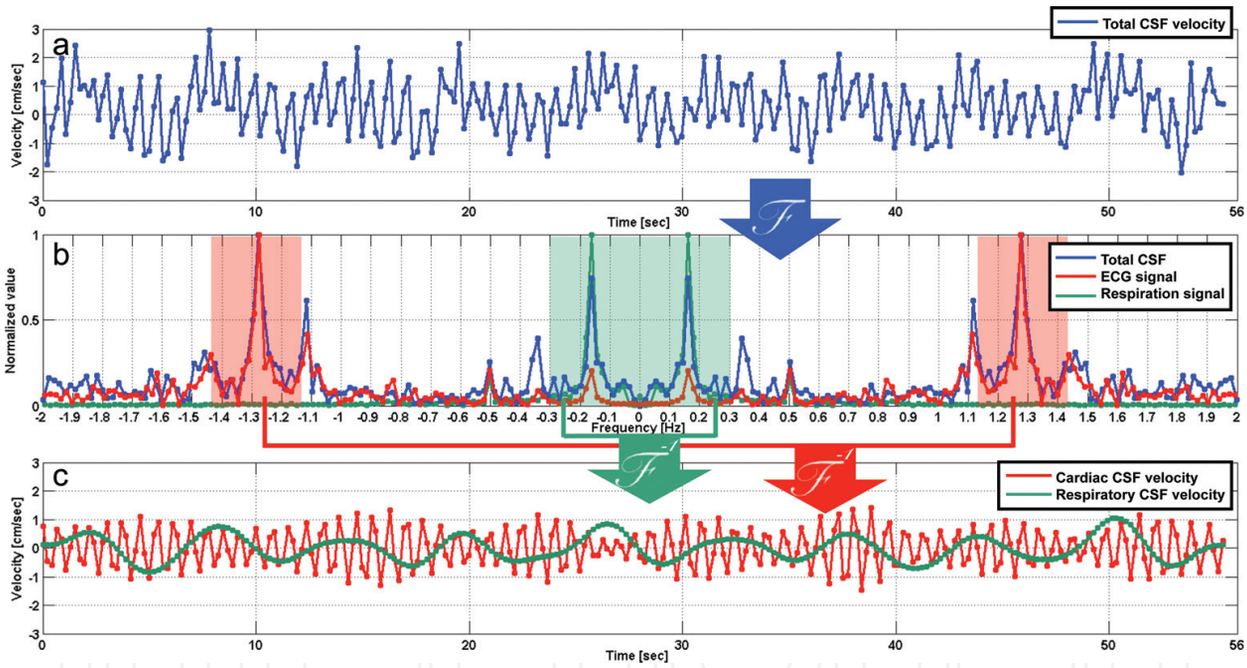

Figure 10. Cardiac- and respiratory-driven CSF velocities were separated from the total velocity by Fourier and inverse Fourier transformations.

of the lateral ventricle, and the pixel brightness was relatively high. In 6-, 10-, and 16-s respiratory cycles, the power ratios between the cardiac- and respiratory-driven components at the anterior cistern of the brainstem are compared in **Figure 12(a)**, while the ratios of quantitative analysis in 6-s respiration are exhibited in **Figure 12(b)**. Significant differences between the cardiac and respiratory energy were observed at all respiratory periods, while the power ratios at 6 s were significantly different in ROIs #1–3. **Table 2** summarizes the average and standard deviation of the cardiac and respiratory fractions for each respiratory cycle. Significant differences were obtained in the same ROIs at various respiratory cycles.

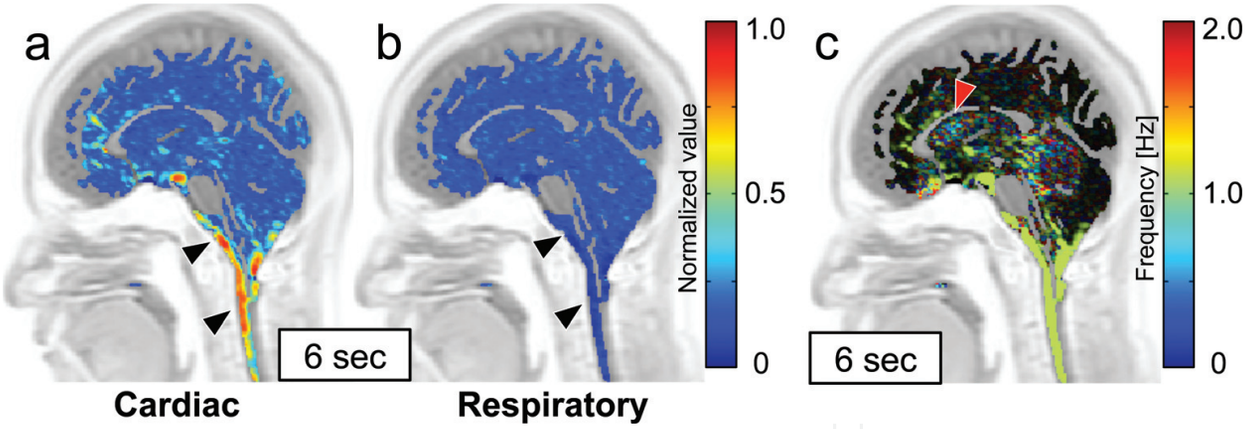

Figure 11. The cardiac (a) and respiratory (b) P-map in a 6-s respiratory period (≈0.167 Hz). The cardiac CSF energy was apparently high at the anterior cistern of the brainstem and spinal subarachnoid space shown by a black arrowhead. (c) An example of an F-map in a 6-s respiratory period. Brightness was changed based on the average of the maximum peaks of CSF power spectra in the CSF space. At the anterior part of lateral ventricle shown by a red arrowhead, this region had mixed various frequencies and relatively high velocities.

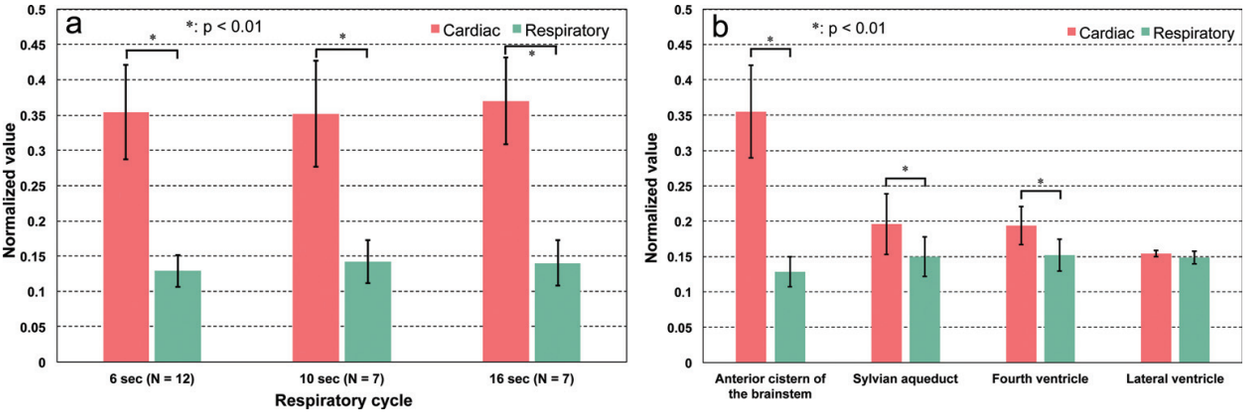

Figure 12. (a) Fractions of the cardiac and respiratory powers with the number of subjects (N) at ROI #1 depicted in **Figure 3**. (b) Fractions of the cardiac and respiratory CSF energies at various ROIs in a 6-s respiratory cycle.

	6 s		10 s		16 s	
	Cardiac	**Respiratory**	**Cardiac**	**Respiratory**	**Cardiac**	**Respiratory**
Anterior cistern of the brainstem	0.355 ± 0.065*	0.127 ± 0.021	0.353 ± 0.072*	0.141 ± 0.030	0.370 ± 0.061*	0.140 ± 0.032
Sylvian aqueduct	0.196 ± 0.043*	0.150 ± 0.028	0.205 ± 0.051*	0.159 ± 0.031	0.208 ± 0.052*	0.145 ± 0.025
Fourth ventricle	0.194 ± 0.027*	0.151 ± 0.023	0.189 ± 0.011*	0.154 ± 0.024	0.192 ± 0.014*	0.149 ± 0.018
Lateral ventricle	0.154 ± 0.005	0.148 ± 0.009	0.152 ± 0.006	0.151 ± 0.007	0.154 ± 0.008	0.147 ± 0.007

*$p < 0.01$
Significant differences were recognized between the cardiac and respiratory components at each respiratory cycle ($p < 0.01$).

Table 2. The energy fractions (average ± SD) at the ROIs in three different respiratory cycles.

Figure 13(a) indicates the typical cardiac pressure gradient image at the maximum positive pressure gradient, while **Figure 13(b)** is that at the negative. **Figure 13(c)** and **(d)** is the same but for the respiratory pressure gradient. Moreover, the results of the quantitative analysis of the cardiac and respiratory pressure gradients were depicted in **Figure 13(e)**. At all the ROIs, significant differences were recognized between the cardiac and respiratory pressure gradients.

The peak-to-peak velocity of the cardiac and respiratory components and the fraction of those were assessed, as shown in **Figure 14**. **Figure 14(a)** presents a significantly higher velocity of the cardiac-driven CSF motion at #1 and #2 than that of the respiratory-driven motion ($p < 0.01$). The fraction in **Figure 14(b)** exhibited the significant differences in all ROIs ($p < 0.01$).

The correlation mapping technique applied to the cardiac- and respiratory-driven CSF motions in a healthy volunteer, as depicted in **Figure 15(a)**, demonstrated a difference in the propagation

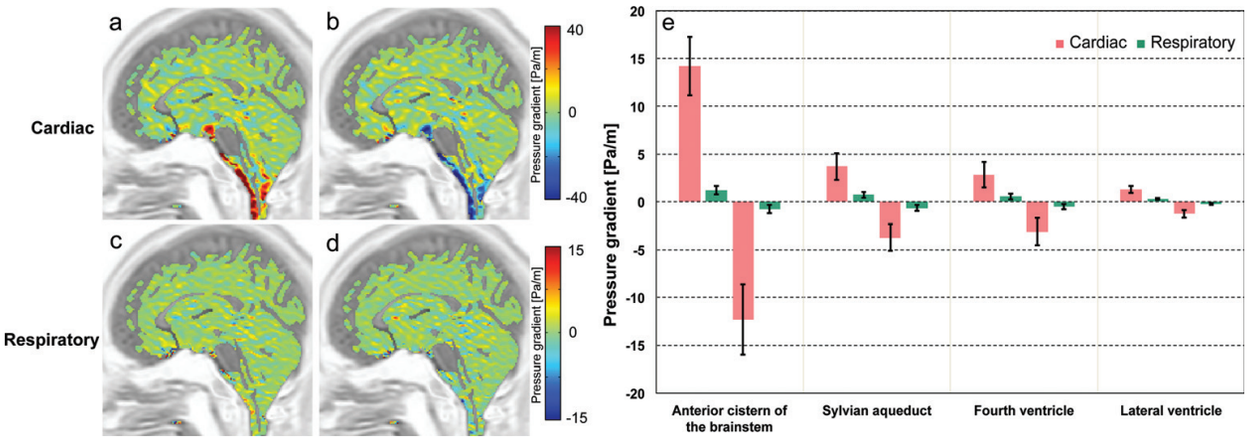

Figure 13. Typical examples of pressure gradient distributions calculated by the separated cardiac- and respiratory-driven CSF velocity. (a) and (b) are the maximum positive and negative gradients of the cardiac, while (c) and (d) are those of the respiratory. In the anterior cistern of the brainstem, the cardiac component was obviously high compared to the respiratory component. (e) Quantitative analysis of the pressure gradients at the ROIs. The upward bars present the positive pressure gradients, while the downward show the negative.

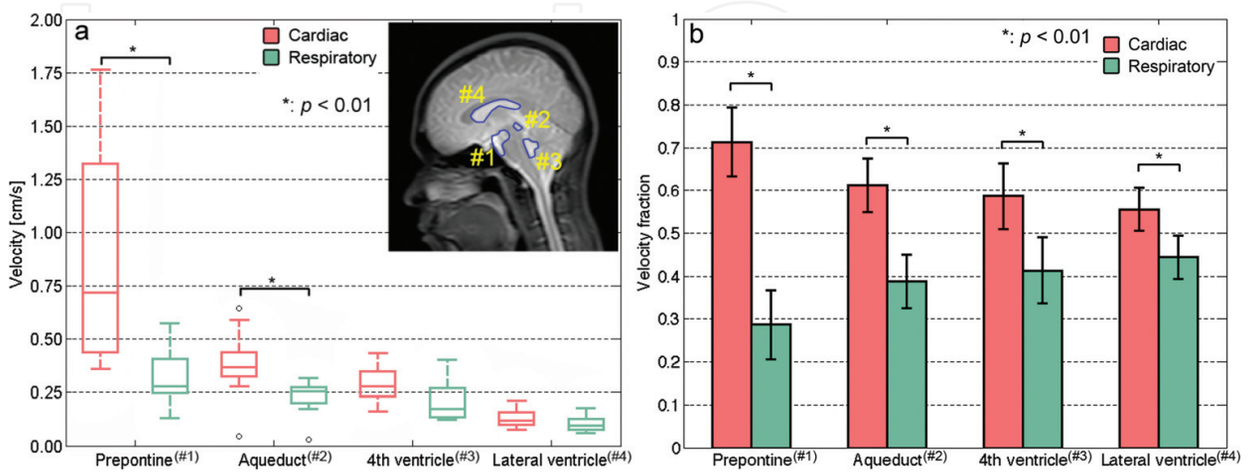

Figure 14. Cardiac- and respiratory-driven CSF velocities were compared at ROIs, the prepontine (#1), aqueduct (#2), fourth ventricle (#3), and lateral ventricle (#4) indicated on T2 images, as shown in (a). The fraction of the cardiac- and respiratory-driven CSF velocities is shown in (b).

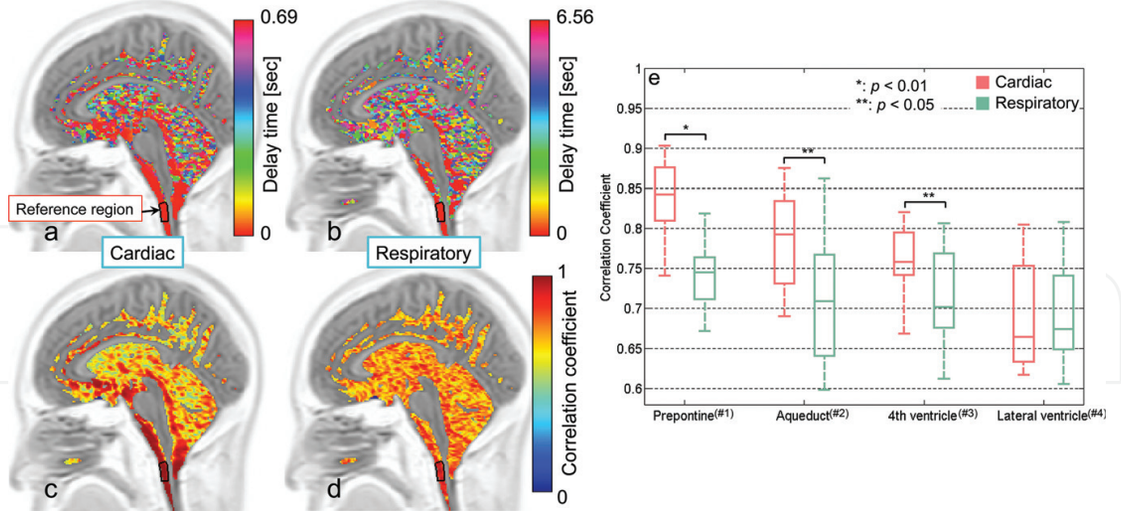

Figure 15. Delay time (a and b) and maximum correlation (c and d) maps of the cardiac- and respiratory-driven CSF velocities for a healthy volunteer; (e) quantitative results of maximum correlation in the ROIs in **Figure 14**. Propagation differences between the cardiac and respiratory were observed.

properties between those motions in intracranial space. The cardiac delay time was short around the brainstem and gradually prolonged with the distance from the reference. In addition, the maximum correlation map indicated a high correlation near the brainstem and low in the midbrain part. The respiratory-driven motion showed scattered delay time distribution and consistently high correlation distribution in contrast to those of the respiratory-driven. The maximum correlation is quantified in **Figure 15(e)**. There are significant cardiac and respiratory differences in #1 ($p < 0.01$), #2 ($p < 0.05$), and #3 ($p < 0.05$).

The CSF displacement, the fraction between the cardiac and respiratory components calculated by the velocity integration, and the displacement modified in accordance with the energy leaking out from the selected band in frequency domain are shown in **Figure 16**. The

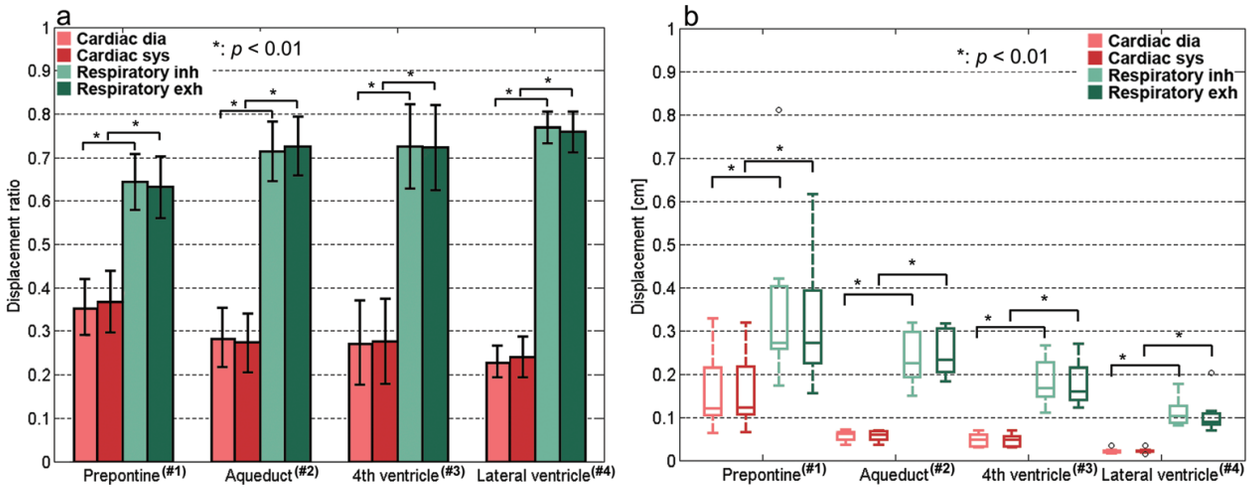

Figure 16. Fractions of the cardiac- and respiratory-driven CSF displacements (a) and the value of displacements modified for the velocity energy leaking out from the selected bandwidth in the frequency domain (b), in the same ROIs as **Figure 14**.

displacement fractions, as well as the displacement values with the energy leak compensation, were significantly larger in the respiratory- than in the cardiac-driven motion in all the ROIs ($p < 0.01$).

4. Discussion

This chapter described techniques to visualize and characterize CSF motion in intracranial space based on PC velocity imaging. They provide quantitative information on CSF motion, which would be useful for clinical diagnosis.

The 4D-VM technique visualized and characterized various quantities of the cardiac-driven CSF motion. The curl images showed the disturbance of motion, and the pressure gradient represented the pressure propagation that may relate to the driving force. The delay time and the maximum correlation exhibited differences in the cardiac-driven CSF motion among the young, healthy, elderly, healthy, and iNPH patient groups. The presence of delay and correlation variations indicates the presence of compliance in the CSF space and brain parenchyma, as CSF is an uncompressible fluid. Brain compliance decreases with age and iNPH status [26, 27]. The velocity, curl, pressure gradient, delay time, and correlation images may reflect hydrocephalus. The limitations of the cardiac-gated PC imaging are the long acquisition duration and the lack of the information on the respiratory-driven motion.

The asynchronous PC technique separated the cardiac- and respiratory-driven CSF motions. The P- and F-maps indicated that the cardiac component is predominant in the anterior cistern of the brainstem. There are major arteries, such as the basilar artery, which may cause the strong cardiac-driven CSF motion around this tissue region. In addition, the cardiac pulsation period is remarkably shorter than that of respiratory pulsation. The instantaneous and strong cardiac pulsation induces a large pressure gradient resulting in the predominant CSF motion in comparison with the cardiac-driven motion. Moreover, velocity analysis as well as correlation mapping exhibited that the cardiac component was significantly larger than the respiratory component. Thus, the difference between the cardiac and respiratory driving forces appeared in power, frequency, delay time and correlation mapping, and displacement analysis based on asynchronous PC imaging. On the other hand, the respiratory-driven displacement was larger than that of the cardiac because the blood volume change induced by respiration is known to be larger than that induced by cardiac pulsation [6]. This suggests that a high velocity of CSF does not necessarily mean large displacement.

The asynchronous PC technique has several limitations, such as its relatively low temporal resolution and ignorance of the bulk flow. The temporal resolution achieved in the present work was 217 ms corresponding to 4.61 frames/s. Acceleration techniques, such as compressed sensing with sparse sampling, may be needed for higher frame rates and thus accurate evaluation of the CSF motion. The bulk flow, whose velocity may be in the order of molecular diffusion, must be investigated to understand the mass transfer or washout mechanisms in the brain.

5. Conclusion

The usefulness of the MR techniques, such as 4D-VM, correlation mapping, power and frequency mapping, and displacement analysis based on cardiac-gated and asynchronous PC imaging, were described.

Acknowledgements

The authors thank Prof. Yutaka Imai and Dr. Koichi Oshio for their valuable discussions. They also thank Mr. Tomohiko Horie and Mr. Nao Kajihara for their assistance in MR imaging.

Conflict of interest

The authors declare they have no conflicts of interest.

Author details

Satoshi Yatsushiro[1], Saeko Sunohara[2], Hideki Atsumi[3], Mitsunori Matsumae[3] and Kagayaki Kuroda[1,2]*

*Address all correspondence to: kagayaki@keyaki.cc.u-tokai.ac.jp

1 Graduate School of Science and Technology, Tokai University, Hiratsuka, Kanagawa, Japan

2 Graduate School of Engineering, Tokai University, Hiratsuka, Kanagawa, Japan

3 Department of Neurosurgery, Tokai University School of Medicine, Isehara, Kanagawa, Japan

References

[1] Bunck AC, Kroger JR, Juttner A, Brentrup A, Fiedler B, Schaarschmidt F, Crelier GR, Schwindt W, Heindel W, Niederstadt T, Maintz D. Magnetic resonance 4D flow characteristics of cerebrospinal fluid at the craniocervical junction and the cervical spinal canal. European Radiology. 2011;**21**:1788-1796

[2] Hirayama A, Matsumae M, Yatsushiro S, Abdulla A, Atsumi H, Kuroda K. Visualization of pulsatile CSF motion around membrane-like structures with both 4D velocity mapping and time-SLIP technique. Magnetic Resonance in Medical Sciences. 2015;**14**:263-273

[3] Horie T, Kajihara N, Matsumae M, Obara M, Hayashi N, Hirayama A, Takizawa K, Takahara T, Yatsushiro S, Kuroda K. Magnetic resonance imaging technique for visualization of irregular cerebrospinal fluid motion in the ventricular system and subarachnoid space. World Neurosurgery. 2017;**97**:523-531

[4] Matsumae M, Hirayama A, Atsumi H, Yatsushiro S, Kuroda K. Velocity and pressure gradients of cerebrospinal fluid assessed with magnetic resonance imaging. Journal of Neurosurgery. 2014;**120**:218-227

[5] Yamada S, Miyazaki M, Kanazawa H, Higashi M, Morohoshi Y, Bluml S, McComb JG. Visualization of cerebrospinal fluid movement with spin labeling at MR imaging: Preliminary results in normal and pathophysiologic conditions. Radiology. 2008;**249**:644-652

[6] Yamada S, Miyazaki M, Yamashita Y, Ouyang C, Yui M, Nakahashi M, Shimizu S, Aoki I, Morohoshi Y, McComb JG. Influence of respiration on cerebrospinal fluid movement using magnetic resonance spin labeling. Fluids Barriers CNS. 2013;**10**:36

[7] Hladky SB, Barrand MA. Mechanisms of fluid movement into, through and out of the brain: Evaluation of the evidence. Fluids and Barriers of the CNS. 2014;**11**:26

[8] Jessen NA, Munk AS, Lundgaard I, Nedergaard M. The Glymphatic system: A Beginner's guide. Neurochemical Research. 2015;**40**:2583-2599

[9] Hayashi N, Matsumae M, Yatsushiro S, Hirayama A, Abdullah A, Kuroda K. Quantitative analysis of cerebrospinal fluid pressure gradients in healthy volunteers and patients with normal pressure hydrocephalus. Neurologia Medico-Chirurgica (Tokyo). 2015;**55**:657-662

[10] Yatsushiro S, Sunohara S, Hayashi N, Hirayama A, Matsumae M, Atsumi H, Kuroda K. Cardiac-driven pulsatile motion of intracranial cerebrospinal fluid visualized based on a correlation mapping technique. Magnetic Resonance in Medical Sciences. 2017. DOI: 10.2463/mrms.mp.2017-0014

[11] Chen L, Beckett A, Verma A, Feinberg DA. Dynamics of respiratory and cardiac CSF motion revealed with real-time simultaneous multi-slice EPI velocity phase contrast imaging. NeuroImage. 2015;**122**:281-287

[12] Dreha-Kulaczewski S, Joseph AA, Merboldt KD, Ludwig HC, Gartner J, Frahm J. Inspiration is the major regulator of human CSF flow. The Journal of Neuroscience. 2015; **35**:2485-2491

[13] Yatsushiro S, Sunohara S, Takizawa K, Matsumae M, Kajihara N, Kuroda K. Characterization of cardiac- and respiratory-driven cerebrospinal fluid motions using correlation mapping with asynchronous 2-dimensional phase contrast technique In: Proceedings of the 38th Annual Meeting of the IEEE Engineering in Medicine and Biology Society. 2016. pp. 3867-3870

[14] Yildiz S, Thyagaraj S, Jin N, Zhong X, Heidari Pahlavian S, Martin BA, Loth F, Oshinski J, Sabra KG. Quantifying the influence of respiration and cardiac pulsations on cerebrospinal fluid dynamics using real-time phase-contrast MRI. Journal of Magnetic Resonance Imaging. 2017;**46**:431-439

[15] Iliff JJ, Wang M, Liao Y, Plogg BA, Peng W, Gundersen GA, Benveniste H, Vates GE, Deane R, Goldman SA, Nagelhus EA, Nedergaard M. A paravascular pathway facilitates CSF flow through the brain parenchyma and the clearance of interstitial solutes, including amyloid β. Science Translational Medicine. 2012;**4**:147ra111

[16] Louveau A, Smirnov I, Keyes TJ, Eccles JD, Rouhani SJ, Peske JD, Derecki NC, Castle D, Mandell JW, Lee KS, Harris TH, Kipnis J. Structural and functional features of central nervous system lymphatic vessels. Nature. 2015;**523**:337-341

[17] Luetmer PH, Huston J, Friedman JA, Dixon GR, Petersen RC, Jack CR, McClelland RL, Ebersold MJ. Measurement of cerebrospinal fluid flow at the cerebral aqueduct by use of phase-contrast magnetic resonance imaging: Technique validation and utility in diagnosing idiopathic normal pressure hydrocephalus. Neurosurgery. 2002;**50**:534-543 discussion 534-543

[18] Parkkola RK, Komu ME, Kotilainen EM, Valtonen SO, Thomsen C, Gideon P. Cerebrospinal fluid flow in patients with dilated ventricles studied with MR imaging. European Radiology. 2000;**10**:1442-1446

[19] Gideon P, Stahlberg F, Thomsen C, Gjerris F, Sorensen PS, Henriksen O. Cerebrospinal fluid flow and production in patients with normal pressure hydrocephalus studied by MRI. Neuroradiology. 1994;**36**:210-215

[20] Pelc LR, Pelc NJ, Rayhill SC, Castro LJ, Glover GH, Herfkens RJ, Miller DC, Jeffrey RB. Arterial and venous blood flow: Noninvasive quantitation with MR imaging. Radiology. 1992;**185**:809-812

[21] Pelc NJ, Bernstein MA, Shimakawa A, Glover GH. Encoding strategies for three-direction phase-contrast MR imaging of flow. Journal of Magnetic Resonance Imaging. 1991;**1**:405-413

[22] Tang C, Blatter DD, Parker DL. Accuracy of phase-contrast flow measurements in the presence of partial-volume effects. Journal of Magnetic Resonance Imaging. 1993;**3**:377-385

[23] Abdullah A, Hirayama A, Yatsushiro S, Matsumae M, Kuroda K. Cerebrospinal fluid image segmentation using spatial fuzzy clustering method with improved evolutionary expectation maximization. In: Proceedings of the 35th Annual Meeting of IEEE Engineering in Medicine and Biology Society; Osaka, Japan. 2013. pp. 3359-3362

[24] Feynman RP, Leighton RB, Sands M. The Feynman Lectures on Physics. 2nd ed. Reading, MA: Addison Wesley; 1970

[25] Alperin N, Lee SH. PUBS: Pulsatility-based segmentation of lumens conducting non-steady flow. Magnetic Resonance in Medicine. 2003;**49**:934-944

[26] Uftring SJ, Chu D, Alperin N, Levin DN. The mechanical state of intracranial tissues in elderly subjects studied by imaging CSF and brain pulsations. Magnetic Resonance Imaging. 2000;**18**:991-996

[27] Bech RA, Waldemar G, Gjerris F, Klinken L, Juhler M. Shunting effects in patients with idiopathic normal pressure hydrocephalus; correlation with cerebral and leptomeningeal biopsy findings. Acta Neurochirurgica. 1999;**141**:633-639